Materials & Design 246 (2024) 113337

Contents lists available at ScienceDirect

Materials & Design

journal homepage: www.elsevier.com/locate/matdes

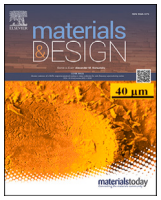

Magnetic alginate microrobots with dual-motion patterns through centrifugally driven flow control

Zihan Wang [a,*], Wenjian Li [b], Chuang Li [a], Anke Klingner [c], Yutao Pei [b], Sarthak Misra [a,d], Islam S.M. Khalil [e,*]

[a] Department of Biomaterials and Biomedical Technology, University of Groningen and University Medical Center Groningen, Groningen, 9713 GZ, the Netherlands
[b] Department of Advanced Production Engineering, Engineering and Technology Institute Groningen, University of Groningen, Groningen, 9747 AG, the Netherlands
[c] Department of Physics, The German University in Cairo, New Cairo, 11835, Egypt
[d] Department of Biomechanical Engineering, University of Twente, Enschede, 7500 AE, the Netherlands
[e] RAM—Robotics and Mechatronics, University of Twente, Enschede, 7500 AE, the Netherlands

ARTICLE INFO

Keywords:
Alginate microrobots
Centrifugally driven flow
Dual-motion patterns
Magnetic actuation
Ultrasound imaging

ABSTRACT

Mobile microrobots have gained increasing attention in biomedical applications because they can be precisely actuated to targeted positions in a tiny space. However, their use in biomedical applications is hindered by the costly and complicated fabrication method. Herein, a facile fabrication method is proposed to produce magnetic alginate microrobots with adjustable dimensions, including teardrop and tadpole shapes, via tunable centrifugally-driven flows. The formation of these microrobots is interpreted by finite element analysis, revealing that the transition between the dripping and jetting regimes of the flow alters the microrobot's shape. The dimensions of the microrobots are quantitatively analyzed based on the flow's extrusion velocity, controlled by nozzle diameters and revolution speeds. Incorporating magnetic nanoparticles into the alginate-based hydrogel enables the microrobots to exhibit distinct motion patterns under a magnetic field. The teardrop-like microrobot can reach a maximum rolling velocity of approximately 2.7 body length s^{-1} at 2 Hz, while the maximum stick-slip velocity of the tadpole-like microrobot reaches about 0.42 body length s^{-1} at 5 Hz, comparable to the existing bioinspired magnetic microrobots. These two motion patterns allow the microrobot to overcome obstacles and navigate in vertically constrained environments, respectively. Last, an ultrasound imaging system is deployed to monitor the locomotion and degradation of the microrobots, showing their potential for targeted drug delivery applications.

1. Introduction

Untethered microrobots are emerging viable tools for minimally invasive medicine due to their miniaturization, maneuverability, and versatility [1–4]. Building on these attributes, the precision operability of untethered microrobots, such as helical microrobots and microrobotic swarms, has been a focus of research over the past few decades. To better navigate complex environments with unpredictable disturbances and obstacles, advanced control strategies have been introduced to refine these microrobots' control precision and performance [5–8]. These advancements in control strategies equip these small-scale robots with the potential to operate in confined spaces and assist surgeons in performing surgeries at hard-to-reach positions. Moreover, their precise operability and capability to transport cargo can address problems in systemic drug delivery, such as poor accumulation at target sites [9], quick emergence of antibiotic resistance [10], and side effects to healthy cells or organs [11]. However, integrating these robots into clinical practice is challenging because technical hurdles and design complexities exist in their fabrication [12,13]. For instance, robots at the macro level are equipped with a suite of sensors, actuators, power sources, and programmable control units, which are difficult to replicate on a microrobot because of size constraints. Biomimicry offers a promising design methodology for the fabrication of microrobots. By mimicking the design principles observed in living microorganisms or cells, microrobots can be endowed with locomotion capabilities [14,15]. These bioinspired microrobots, with their bionic characteristics, are also designed to interact with the surrounding environments and even camouflage without alarming other creatures [16]. Furthermore, the biomimetic principles applied in the

* Corresponding authors.
E-mail addresses: z.wang04@umcg.nl (Z. Wang), i.s.m.khalil@utwente.nl (I.S.M. Khalil).

https://doi.org/10.1016/j.matdes.2024.113337
Received 4 June 2024; Received in revised form 20 September 2024; Accepted 24 September 2024
Available online 27 September 2024

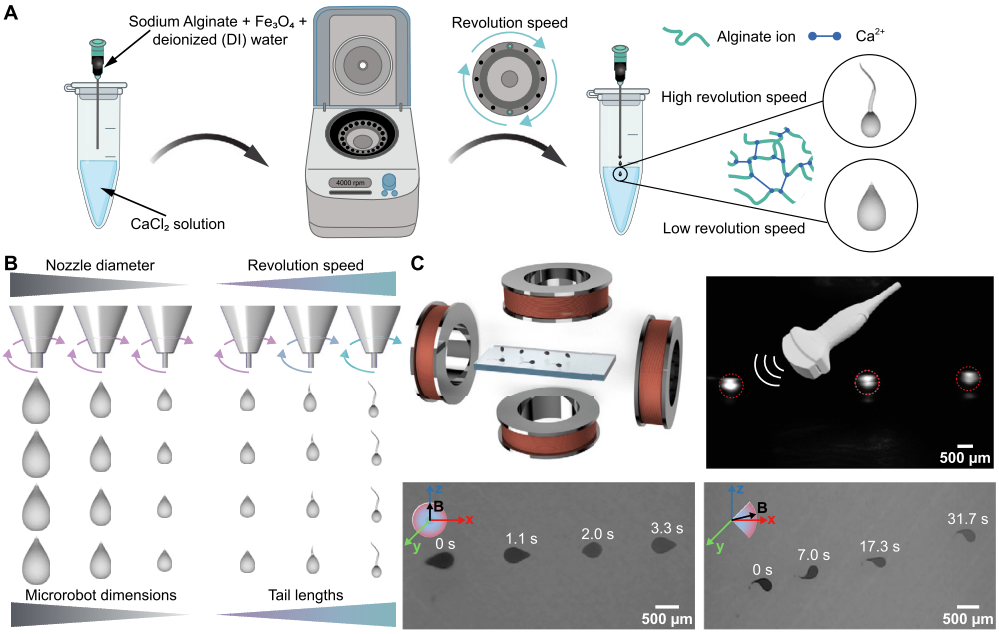

Fig. 1. Fabrication, actuation, and imaging of magnetic alginate microrobots. (A) Magnetic alginate microrobots, including teardrop and tadpole shapes, are fabricated through centrifugally driven flow and cross-linking method using Ca^{2+} ions. (B) The shapes and dimensions of the microrobots are adjusted by varying the revolution speed of a centrifuge and the diameter of a nozzle. (C) Magnetic actuation is conducted in an electromagnetic coil system. The micrographs show the rolling motion of a teardrop-like microrobot under a rotating field and the stick-slip motion of a tadpole-like microrobot under an oscillating field. The ultrasound (US) image shows three teardrop-like microrobots at the wall of a water tank.

design of helical microrobots have been modified to include a sharp cutting tip, which allows them to mechanically eliminate blood clots effectively [17].

Natural organisms, such as fish, tadpoles, and sperm, achieve locomotion by undulating their tails. Bioinspired microrobots have been designed to replicate this locomotion mechanism through various fabrication methods, including photolithography [18,19], electrodeposition [20], and direct laser writing [21]. Tadpole-like microrobots, consisting of a head of magnetic microbead and a tail of magnetic nanoparticles chain, have been constructed using a magnetically assisted in situ polymerization method. This process involves magnetizing a microbead and attracting magnetic nanoparticles via magnetic forces to form a chain. The as-prepared tadpole-like structure is encapsulated within a hydrogel following ultraviolet polymerization [22]. Tan et al. have reported a one-step formation method for sperm-like magnetic microrobots by developing a vortex turbulence-assisted microfluidics platform [23]. Monodispersed magnetic alginate/oil droplets are first formed within the microfluidics platform. Subsequently, a slender tail is extracted from the droplets due to the vortex flow generated by a rotational magnetic stirrer. In addition, sperm-like microrobots have been fabricated by cutting electrospun beaded fibers into segments where the bead and fiber serve as the head and the tail, respectively [24]. These bioinspired microrobots can move forward through the undulatory propulsion of their tails, akin to the swimming of fish, tadpoles, and sperm. Despite considerable efforts to advance fabrication methods for magnetic bioinspired microrobots, challenges persist within the mentioned methods. The existing fabrication methods, involving tedious procedures and expensive equipment, are not suitable for mass production.

Microfluidics is a promising microfabrication technique that has wide-ranging applications in biology [25], chemistry [26], medical diagnostics [27], and engineering [28]. In the design of microfluidic devices, pumps are crucial for moving fluid through narrow channels. Centrifugal pumps provide many advantages, including the ability to handle highly viscous liquids, operate without introducing bubbles, and ease of accessibility. In this study, we demonstrate the bulk fabrication of magnetic alginate microrobots, including teardrop and tadpole shapes, through centrifugal pumping. These microrobots are produced by finely controlling centrifugally driven flows and subsequent cross-linking of the magnetic alginate solution (Fig. 1A). The shapes and dimensions of the microrobots are tailored by adjusting the flow velocity, impacted by nozzle diameters and the centrifuge's revolution speeds (Fig. 1B). Increasing flow velocity induces a transition from the dripping phase, where droplets form, to the jetting phase, which produces elongated jets. These droplets and jets serve as the head and tail of the microrobots, respectively. Characterizations are conducted to assess their morphologies, dimensions, chemical composition, and locomotion capabilities. The adoption of magnetic actuation ensures operational safety by eliminating the need for harmful chemical fuels. Lastly, the imaging by the ultrasound imaging system and the degradation experiments are conducted, showcasing our microrobots' potential for precise drug delivery in clinical settings (Fig. 1C).

2. Materials and methods

2.1. Preparation and gelation of magnetic alginate solution

The concentration of 4% w/v sodium alginate solution was prepared using the following procedure. First, 0.6 g Alginic acid sodium salt from brown algae (71238-250G, Sigma-Aldrich, The Netherlands) was dissolved in 15 mL of deionized (DI) water. The mixture was magnetically stirred for 3 hours in an oil bath at a speed of 500 rpm and a temperature of 45 °C. Then 0.25 g Fe_3O_4 (637106-25G, Sigma-Aldrich, The Netherlands) was added to the prepared solution and uniformly dispersed using sonication. The gelation of magnetic alginate solution occurred in 5% w/v $CaCl_2$ solution, which was prepared by dissolving 2 g of calcium chloride dihydrate (223506-25G, Sigma-Aldrich, The Netherlands) in 40 mL DI water. The contact with $CaCl_2$ solution was facilitated via centrifugal pumping, where the centrifugal force was provided by a centrifuge (5417 R, Eppendorf, The Netherlands). In the experiments, the centrifuge's revolution speeds varied from 1000 to 7000 revolutions per minute (rpm). The corresponding relative centrifugal forces (also referred to as G force) for each speed were as follows: 1000 rpm (106 G), 2000 rpm (425 G), 3000 rpm (956 G), 4000 rpm (1699 G), 5000 rpm (2655 G), 6000 rpm (3824 G), and 7000 rpm (2824 G).

2.2. Viscosity and oscillatory shear rheology measurement

The dynamic viscosity and oscillatory shear rheology measurement of magnetic alginate solution and hydrogel were performed at room temperature (25 °C) using a rheometer (MCR 92, Anton Paar, The Netherlands) with a parallel-plate geometry (PP25, diameter: 25 mm). Shear rates ranging from 0.01 s^{-1} to 1000 s^{-1} were applied to the solution, and the rheometer recorded the resulting shear stress. The dynamic viscosities of the solution were calculated through the ratio of shear stress to shear rate. In addition, an oscillatory test was conducted to investigate the viscoelastic behavior of the solution and the hydrogel. Amplitude sweeps were carried out to measure the storage and loss moduli. The shear strain range was set from 0.1% to 1000% for the solution and from 0.01% to 10% for the hydrogel, with an oscillatory frequency of 1 Hz.

2.3. Pendant drop method

The surface tension of the magnetic alginate solution was measured using the pendant drop method. A three-prong clamp secured a syringe filled with the solution to a vertical support rod. A camera (D5600, Nikon Corporation, Japan) with a lens (AF-S 18-140 mm, Nikon Corporation, Japan) was utilized to record the deformation of a droplet suspended at the tip of the syringe. The droplet's shape is determined by the balance of the surface tension force and the gravitational force acting on the droplet. The equation that estimates the surface tension σ can be given by, $\sigma = \frac{\Delta\rho g D_E^2}{H}$, where $\Delta\rho$ is the density difference between the magnetic alginate solution and air, g is the gravitational constant, D_E is the maximum diameter of the pendant droplet, and H characterizes the deformation of the droplet due to gravity [29].

2.4. SEM characterization

Prior to SEM characterization, the magnetic alginate microrobots were prepared through fixation, dehydration, and freeze-drying. The fixation was conducted overnight in 2.5% glutaraldehyde solution (diluted in 50% glutaraldehyde solution, 340855-25ML, Sigma-Aldrich, The Netherlands). The microrobots were dehydrated using a series of ethanol gradients (25%, 50%, 75%, 100%) following the fixation. Subsequently, the dehydrated samples were transferred to a freezing dryer with a temperature of -108 °C and a pressure below 5 mPa. The as-prepared samples were mounted in the carbon tape for further SEM observation (Lyra 3 XM, Tescan, Czech Republic). Finally, the microrobots were analyzed using SEM imaging and EDS elemental mapping at an electron beam voltage of 7 KV. To enhance their conductivity, a 20 nm thick layer of gold was deposited on the microrobots.

2.5. Experimental setup

The locomotion experiments of the magnetic alginate microrobots were carried out in an electromagnetic coil system, which can generate a uniform magnetic field of up to 50 mT at its center. The currents applied to the electromagnetic coils were produced and amplified using the XenusPlus EtherCAT (XE2-230-20, Copley Controls, Canton, USA). This current output system was controlled by a C++—based program. The locomotion of the microrobots was recorded at a rate of 25 frames per second using a microscopic observation setup, which consisted of a charge-coupled device camera (AVA1000-100GM, Basler AG, Ahrensburg, Germany) and an optical microscope with a 2x objective lens. To conduct ultrasound imaging of the microrobots' motion and degradation, the experiment setup was comprised of an ultrasound imaging system (L14-5 scanner, Ultrasonix Medical Corporation, Canada), a water tank including the magnetic microrobots, and a permanent NdFeB magnet. The imaging probe held by a robot arm (Research 3, Franka Emika, Germany) was obliquely submerged into the water tank with an image frequency of 14 MHz and a depth of 1 cm. The permanent magnet was driven by a stepper motor, providing a rotating magnetic field to actuate the microrobots.

2.6. Finite element analysis

Finite element analysis is conducted in COMSOL Multiphysics (version 6.2, COMSOL AB, Sweden) to investigate flow profiles of the microrobots, as well as the formation of teardrop-like and tadpole-like flows. The modules and boundary conditions are indicated below for each simulation result. In Fig. 2A, laminar flow, level set, and multiphysics modules were utilized to simulate the formation of teardrop-like and tadpole-like flows. The laminar flow module featured an inlet at the top of the nozzle and an outlet at the bottom of the centrifuge tube. To facilitate the flow extrusion, we introduced a volume force that simulated centrifugal force and varied with revolution speeds. The level set module assigned initial values 1 to the air phase ($0 < \varphi < 0.5$) and initial values 2 to the liquid phase ($0.5 < \varphi < 1$). The initial interface was positioned at the nozzle tip. Within the multiphysics module, the properties (including density and dynamic viscosity) of air and the magnetic alginate solution were specified, and the surface tension coefficient was measured using the pendant drop method. To simulate the extrusion velocities depicted in Figs. 2C and S3, the laminar flow module was employed. The inlet was set at the top of the nozzle, and the outlet was positioned at the nozzle tip. As part of the initial boundary conditions, the volume force was introduced to simulate the centrifugal force, which was adjusted according to the revolution speeds. The nozzle model was calibrated to match the actual dimensions of real needles. A Laminar flow module was utilized to simulate the flow profiles in Figs. 5B, S9B, and S10. The boundary conditions specified an inlet at the left boundary of the pipe and an outlet at the right boundary, with zero inlet flow velocity applied. Moving mesh settings included a deforming domain and prescribed deformation to represent rolling and stick-slip motions. For the rolling motion, the angle α between the major axis along the Feret diameter and **x** axis varied as $\alpha = 2\pi f t$, where f represented the rotating frequency. The stick-slip motion involved an oscillating pattern, with the angle α varying as $\alpha = A * \sin(2\pi f t)$, where f was the oscillating frequency and A was the maximum oscillating angle. To implement these motion patterns, we prescribed the deformation using the equation $dx = ((\cos\alpha - 1) * X + (-\sin\alpha) * Y, \sin\alpha * X + (\cos\alpha - 1) * Y)^T$, where (X, Y) represents the coordinates of the microrobots at the previous time instant.

3. Results and discussions

3.1. Fabrication of magnetic alginate microrobots

Sodium alginate is selected as the material of the microrobots due to its biocompatible and biodegradable properties [30]. A facile method is proposed to fabricate the microrobots, as shown in Fig. 1A. The alginate solution mixed with Fe_3O_4 nanoparticles is pumped from the nozzle by centrifugal forces and subsequently comes into contact with the $CaCl_2$ solution within a centrifuge tube. This contact initials the gelation process, where the liquid alginate solution transforms into a solid gel. During this process, Ca^{2+} ions form links between alginate chains to create a three-dimensional network. The existence of magnetic nanoparticles enables the actuation of microrobots in a magnetic field. Note that the centrifugally driven flow, and consequently the shape and the dimension of the microrobot, can be controlled by adjusting the revolution speeds of the centrifuge. The variability of the revolution speeds allows for the fabrication of teardrop-like and tadpole-like microrobots.

3.2. Characterization and formation simulations of magnetic alginate microrobots

Several factors, including viscoelasticity, density, surface tension, and flow velocity of the magnetic alginate solution, play an important

role in droplet formation when the solution is centrifugally expelled from the nozzle. A rheological study is conducted on the solution to investigate its viscosity and viscoelasticity (see Materials and Methods). Shear stress on the solution was measured with a rheometer across a range of shear rates, as exhibited in the red curve of Fig. S1A. Dynamic viscosities of the solution, calculated from the slope of the red curve, are depicted in the blue curve. The magnetic alginate solution is characterized by decreasing viscosities with increasing shear rates, indicating its shear-thinning behavior. Fig. S1B-I shows the storage modulus (G') and loss modulus (G'') of the solution. The viscous behavior of the solution dominates its elastic behavior, as indicated by the fact that G'' exceeds G'. Fig. S1B-II displays the viscoelastic behavior of the magnetic alginate hydrogel. The storage modulus (G') and the loss modulus (G'') significantly increase after the sol-gel transition. Upon reaching a critical shear stress, microcrack formation occurs in the gel, increasing G'' after the plateau. This is because the broken bridge fragments in the gel move and generate internal viscous friction. With the continuously increasing shear stress, the microcracks grow and merge into a macro crack. The entire gel begins to flow and the viscosity of the gel will exceed its elasticity. In addition, the density of the solution is determined by weighing the solution with a known volume, while the surface tension of the magnetic alginate solution is measured using the pendant drop method (see Materials and Methods and Fig. S2). The molecules in the solution exhibit strong cohesive forces, facilitating the formation of a spherical flow. However, the centrifugal force distorts the spherical shape to a prolate ellipsoid. The finite element analysis method, which considers the interplay between liquid and air phases and the impact of centrifugal force, is essential to comprehend the formation mechanism of the magnetic alginate microrobots.

Level set methods have been employed in various applications such as incompressible two-phase flows [31], viscoelastic fluid flows [32], and fluid-structure interactions [33]. In this study, we utilize the two-phase level set method to track the moving liquid interface [34,35]. The two-phase level-set equation is given by,

$$\frac{\partial \varphi}{\partial x} + \mathbf{u} \cdot \nabla \varphi = \gamma \nabla \cdot \left(\varepsilon \nabla \varphi - \varphi(1-\varphi) \frac{\nabla \varphi}{|\nabla \varphi|} \right). \tag{1}$$

Here $\mathbf{u}$ is the flow velocity, and the level set function, φ, which ranges from 0 to 1, indicates the phase: values below 0.5 denote the air phase, and those above 0.5 indicate the liquid phase. The parameter γ denotes the reinitialization parameter, while ε controls the thickness of the interface. Additionally, the dynamics of the magnetic alginate solution during centrifugal pumping is governed by the following equations,

$$\begin{aligned} \rho \frac{\partial \mathbf{u}}{\partial t} + \rho(\mathbf{u} \cdot \nabla)\mathbf{u} &= \nabla \cdot \left[-p\mathbf{I} + \mu \left(\nabla \mathbf{u} + (\nabla \mathbf{u})^T \right) \right] + \mathbf{F}_{st} + \mathbf{F}_c \\ \nabla \cdot \mathbf{u} &= 0, \end{aligned} \tag{2}$$

where ρ is the solution's density, t is time, p is pressure, $\mathbf{I}$ is the identity matrix, μ is the viscosity of the solution, $\mathbf{F}_{st}$ is the surface tension force, $\mathbf{F}_c$ is the centrifugal force exerted on the solution. These forces can be expressed by the following equations,

$$\mathbf{F}_{st} = \pi d_n \sigma \hat{\mathbf{n}}, \qquad \mathbf{F}_c = -m\omega^2 r \hat{\mathbf{n}}, \tag{3}$$

where d_n is the diameter of the nozzle, σ is the surface tension of the solution, $\hat{\mathbf{n}}$ is the unit vector along the axial direction of the nozzle, m is the mass of the extruded liquid, ω is the revolution speed of the centrifuge, r is the distance of the solution from the central axis of rotation, and $\omega^2 r$ represents the relative centrifugal force.

After substituting Equation (3) into Equations (1) and (2) and solving the governing equations, the extrusion of the magnetic alginate solution from the nozzle was simulated. The simulation depicts the emergence of teardrop-like and tadpole-like flows under varying revolution speeds, as illustrated in Fig. 2A. The dripping and jetting regimes of the flow contribute to its final morphology. During the dripping regime, a pendant droplet forms at the nozzle tip when the centrifugal force is applied. This droplet grows in size due to the continuous supply of the solution. The surface tension force acts to minimize the droplet's surface area, whereas the centrifugal force attempts to detach the droplet from the nozzle tip. The break-off of the droplet occurs when the centrifugal force balances the surface tension force. In the jetting regime, the droplet extends to a long tail owing to the increasing centrifugal force. Viscous resistance resists the elongation and break-off of the tail, thus stabilizing the extruded flow's shape. On the contrary, the Plateau-Rayleigh instability would lead to thinning of the flow at the tail segment. The break-off of the flow occurs when the viscous resistance can no longer maintain the integrity of the tail [36]. Lastly, the tail partially retracts back into the droplet, which is influenced by both the flow velocity and the elasticity of the solution. Fig. 2A-I and II illustrates the simulated flow obtained at low and high revolution speeds, respectively. The surface tension and the centrifugal force result in the formation of a droplet flow, as displayed in Fig. 2A-I. Subsequently, a short tail emerges because the low revolution speed brings about limited fluid volume ejected from the nozzle. This tail retracts owing to elastic and inertial forces within the fluid. Ultimately, a teardrop flow is produced and becomes a gel after contact with $CaCl_2$ solutions. At the high revolution speed, the droplet is initially formed, and then the tadpole-like flow with the longer tail is extruded until the Plateau-Rayleigh instability occurs. The tail retraction is negligible compared to its overall length, as depicted in Fig. 2A-II. Our simulations indicate that as the revolution speed increases, the flow transitions from the dripping to the jetting regime, resulting in a shift from teardrop-like to tadpole-like flows.

Guided by the simulation results, we fabricated the magnetic alginate microrobots by varying nozzle diameters and revolution speeds. Fig. 2B presents the micrographs and phase diagram of microrobots under various experimental conditions. As the revolution speeds increase, the microrobots transform through three stages: teardrop-like microrobots, tadpole-like microrobots, and clusters. Shape transitions of the microrobots come at varying revolution speeds depending on the nozzle diameters. During the fabrication, the needles with diameters of 159 μm (30 gauge), 260 μm (26 gauge), and 413 μm (22 gauge) are used and referred to as S-, M-, and L-sized nozzles below. The teardrop-like and tadpole-like microrobots were fabricated using the L-sized nozzle at revolution speeds of 1000 and 2000 revolutions per minute (rpm), respectively, as indicated by the black circle and red triangle symbols in the phase diagram. The blue square symbols denote the formation of clusters. Using the M-sized nozzle, the shift from the tadpole-like microrobots to undesired clusters occurs at 5000 rpm. To avoid the formation of clusters, the revolution speed should be kept below 6000 rpm when utilizing the S-sized nozzle. Notably, the change in nozzle diameters and revolution speeds results in the variation of the flow's extrusion velocity V_{out} at the nozzle tip. Fig. S3 details the V_{out} using the S-, M-, and L-sized nozzles at 1000 rpm. The extrusion velocity has the highest value at the center of the cross-section and decreases to zero at the nozzle walls due to the no-slip boundary condition. The maximum velocity is used to represent the extrusion velocity. The heatmap in Fig. 2C correlates the simulated extrusion velocity with experimental conditions. After analyzing these results with the phase diagram, we determined that the shift from the teardrop-like microrobots to the tadpole-like microrobots occurs at extrusion velocities between 1.7 mm/s and 3.0 mm/s. Moreover, the heatmap indicates that the undesired clusters are produced when the extrusion velocity exceeds 13.9 mm/s. The extruded velocities of the different nozzles at varying revolution speeds have been theoretically studied. These simulations can thus guide the fabrication process, allowing for the prediction of microrobot shapes under varying experimental conditions (see the regions surrounded by the colored lines in Fig. 2C).

The extrusion velocity not only shapes the microrobots but also impacts the yield of the microrobots. Table S1 displays the yield of magnetic alginate microrobots under different experimental conditions, ranging from 5 to 12,000 per minute. This variance demonstrates a positive correlation with the extrude flow velocity simulated in Fig. 2C,

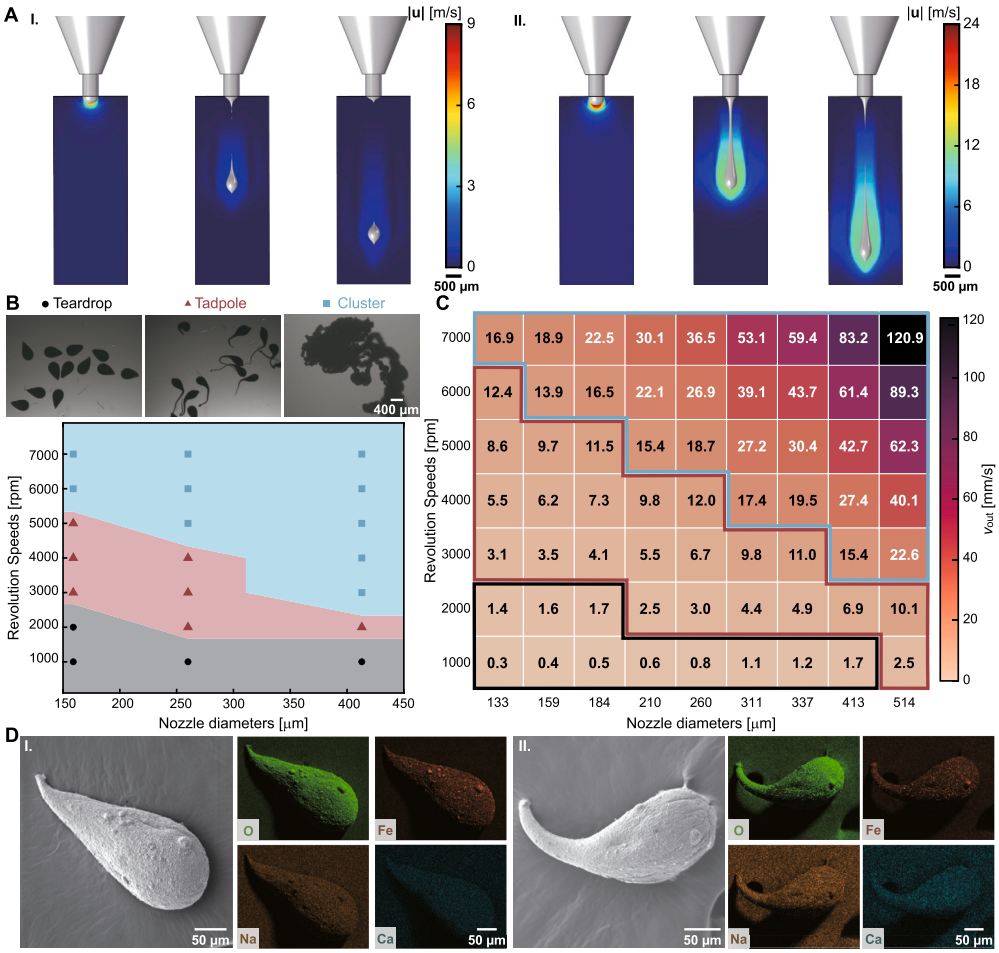

Fig. 2. Characterization, phase diagram, and simulation results (see Materials and Methods). (A) Simulation results show the formation of (I) a teardrop-like flow and (II) a tadpole-like flow over time. The colormap represents the flow velocity **u**. (B) Micrographs and phase diagram of the magnetic alginate microrobots with different morphologies under varying experimental conditions. (C) The heatmap depicts the extrusion velocity V_{out} at the nozzle tip under different experimental conditions. The values within the rectangular box represent the predicted extrusion velocity v_{out} under the corresponding experiment conditions. (D) Scanning electron microscope (SEM) imaging and energy-dispersive X-ray spectroscopy (EDS) elemental mapping images of O, Fe, Na, and Ca in (I) the teardrop-like and (II) the tadpole-like microrobots.

indicating that higher extrusion velocities facilitate greater yield. To clarify the influence of the extrusion velocity on the microrobots' morphology, Fig. 2D presents scanning electron microscope (SEM) images that feature the teardrop-like and tadpole-like microrobots. Notably, the tadpole-like microrobot shown in the SEM image was produced at a lower revolution speed compared to that in the micrograph. Moreover, the dehydration process during SEM sample preparation can lead to shrinkage of the magnetic alginate microrobots. Thus, the tail lengths of the tadpole-like microrobots in the SEM and optical brightfield micrographs are distinct. A zoom-in SEM image on the tail of a tadpole-like microrobot and the corresponding EDS elemental mapping images of Na and Ca are presented in Fig. S4. The Na EDX signals are less distinct from the grid background, which we attribute to the relatively small amount of Na element in the robots, as most Na^+ are replaced by Ca^{2+} during the gelation process. The presence of Fe_3O_4 clusters on the surface of the magnetic microrobot is indicated by the enlarged SEM image in Fig. S5A. In conjunction with these observations, energy-dispersive X-ray spectroscopy (EDS) mapping analysis reveals the coexistence of O, Fe, Na, and Ca elements. The elemental analysis in Fig. S5B demonstrates an atomic percentage of 73.55% C, 22.75% O, 1.06% Fe, and 2.64% Ca. The weight ratio of Fe_3O_4 within the microrobot is calculated to be around 5.79%.

3.3. Size scalability of magnetic alginate microrobots

To understand the effect of the nozzle diameters and the revolution speeds on microrobot dimensions, we analyzed teardrop-like and tadpole-like microrobots produced under various conditions. The dimension of these microrobots decreases as the inner diameter of the nozzle narrows, as shown in the SEM micrographs of Fig. 3A and the optical brightfield micrographs of Fig. S6A. Moreover, increasing the revolution speeds results in the tail elongation of tadpole-like microrobots (see Fig. 3B and Fig. S6B). Hence, it is essential to understand the relationship between the dimensions of these microrobots and experimental conditions.

Two terms regarding the dimension of the magnetic alginate microrobots, Feret diameter, and MinFeret diameter, are first introduced. The Feret diameter of the microrobot refers to the longest distance between any two points along the perimeter of the tadpole-like microrobot's head or the teardrop-like microrobot, also known as the maximum caliper diameter. The MinFeret diameter represents the minimum caliper diameter. These dimensions of the microrobots obtained via the corresponding experimental conditions are displayed in the first two columns of Fig. 4A. At a revolution speed of 1000 rpm, the Feret diameters averagely decrease from 649 μm to 420 μm, and the average MinFeret diameters decline from 374 μm to 321 μm across the L-, M-, and S-sized

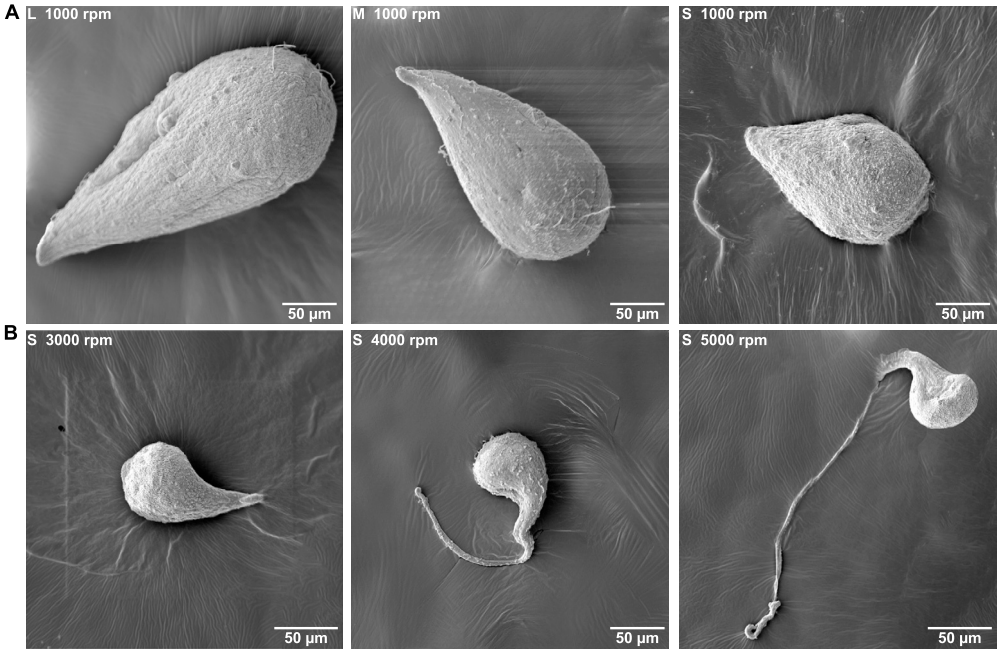

Fig. 3. SEM images of (A) teardrop-like microrobots fabricated using the L-, M-, and S-sized nozzles at 1000 rpm, and (B) tadpole-like microrobots fabricated using the S-sized nozzle at increasing revolution speeds (including 3000 rpm, 4000 rpm, and 5000 rpm). The L-, M-, and S-sized nozzles refer to the 22-, 26-, and 30-gauge needles, respectively, with the diameters of 413 μm, 260 μm, 159 μm.

nozzles. With a fixed nozzle diameter, both the Feret and the MinFeret diameters decrease as the revolution speed increases.

As previously mentioned, the droplet breaks off when the centrifugal force equals the surface tension force. Assuming a sphere flow detaches from the nozzle tip, the diameter d_{sphere} of the spherical flow can be determined by the following equation [37],

$$d_{\text{sphere}} = \sqrt[3]{\frac{6d_{\text{n}}\sigma}{\rho\omega^2 r}}. \tag{4}$$

The predicted diameters of the spherical flow across various revolution speeds using the L-, M-, and S-sized nozzles are plotted as black lines in Fig. 4B. A noticeable deviation is observed in comparison to the experimental data highlighted by blue and red error bars. To accurately reflect the dimensions of the microrobots, the calibrated coefficients a_{max} and a_{min} are introduced to account for the shrinkage of the droplet in the directions of the Feret and the MinFeret diameters, respectively. This shrinkage can be attributed to the volume loss during the gelation of the alginate solution. The revised equation for estimating the Feret and the MinFeret diameters of the microrobot is as follows,

$$d_{\text{x}} = (1 - a_{\text{x}})\sqrt[3]{\frac{6d_{\text{n}}\sigma}{\rho\omega^2 r}}, \quad (\text{x} = \text{min}, \text{max}). \tag{5}$$

The fitted blue and red lines in Fig. 4B, representing the predicted Feret and MinFeret diameters, respectively, closely align with the experimental data. The shrinkage coefficients a_{max} are determined to be -0.0808, 0.0173, and 0.0373 for the microrobots fabricated with the L-, M-, and S-sized nozzles. The value approximately 0 of a_{max} denotes nearly zero shrinkage in the direction of the Feret diameter. Conversely, the shrinkage coefficients a_{min}, derived from the red lines' fitting, have values of 0.3282, 0.2387, and 0.2203, which imply an approximate 26% shrinkage along the MinFeret diameter. The values derived from the formula combining these coefficients, $1-(1-a_{\text{max}})(1-a_{\text{min}})^2$, are calculated to be 51.22%, 43.04%, and 41.47%, reflecting the volume shrinkage of the microrobot's volume after the gelation. Further analysis, depicted in Fig. S7, reveals additional relationships between nozzle diameter and microrobot dimensions. The shrinkage coefficients along the Feret diameter, a_{max}, are -0.0553 and 0.0575 for the microrobots fabricated under 1000 and 2000 rpm, respectively. The shrinkage coefficients along the MinFeret diameter, a_{min}, have values of 0.3193 and 0.2682. These shrinkage ratios along the Feret and MinFeret diameters are in good agreement with the values calculated from the curves in Fig. 4B. The calculated volume shrinkage of the microrobots after gelation is 51.10% and 49.53%, respectively, when fabricated at 1000 and 2000 rpm. This characteristic is impacted by the concentration of magnetic alginate solution and $CaCl_2$ solution. With the assumption of consistent volume shrinkage after the gelation, our findings enable the prediction of magnetic alginate microrobots' Feret and MinFeret diameters under various experimental conditions.

The tail lengths of the tadpole-like microrobots are measured and presented in the frequency histograms, which are fitted with the Gaussian distribution (represented by solid lines in the third column of Fig. 4A). It is observed that the tail lengths increase with the revolution speeds when the nozzle diameter remains constant. In particular, the average tail length of the tadpole-like microrobot is 457 μm using the L-sized nozzle at 2000 rpm. With the M-sized nozzles, this length ranges from 85 μm to 697 μm as revolution speeds rise. For the S-sized nozzles, the increase is from 51 μm to 447 μm. The pinch-off of the flow from the nozzle occurs when the centrifugal force overcomes the viscous resistance and the surface tension force. This results from the appearance of a thin neck in the flow, which ultimately collapses due to Plateau-Rayleigh instability. A quantitative relationship between the tail length and the experimental conditions is challenging to formulate since the forces involved in this process are difficult to predict with analytical models. Thus, only the positive correlation of the tail length with revolution speeds is reported.

3.4. Locomotion capability of magnetic alginate microrobots

The demonstrated scalability of our fabrication method allows for tailoring microrobots' dimensions, which are critical for their locomotion capabilities under magnetic fields. The locomotion experiments of the magnetic alginate microrobots are conducted in a glass petri dish filled with deionized water. When actuated by a uniform magnetic field with a strength of 25 mT, these microrobots settle near the wall of the petri dish (see Materials and Methods and Movie S1). For the

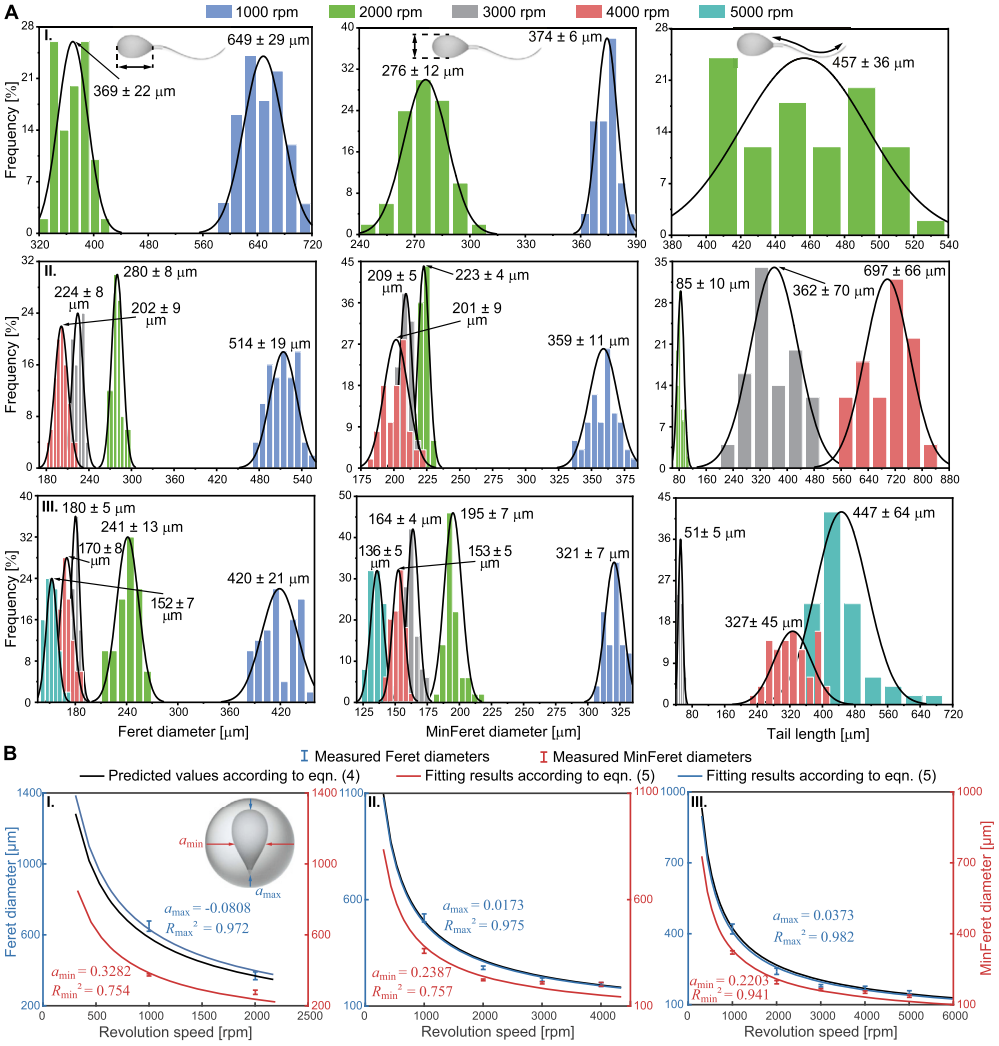

Fig. 4. Size distribution of teardrop-like and tadpole-like microrobots. (A) Frequency histograms show Feret diameters, MinFeret diameters, and tail lengths of the microrobots fabricated using the (I) L-, (II) M-, and (III) S-sized nozzles (n = 50 for each figure). Histograms are fitted with Gaussian distribution (solid lines), and the data is given by mean ± standard deviation. (B) The relationship between the revolution speeds and the Feret diameters, the MinFeret diameters of the microrobots obtained via (I) the L-, (II) M-, and (III) S-sized nozzles. The black curves represent the fitting results through Equation (4). The blue and red curves are the best-fit lines through Equation (5) according to the measured values marked by error bars. The fitting extent is expressed through the value of R_x^2 (x = min, max), while a_x represents the shrinkage ratio of the extruded alginate solution after the gelation, as shown in the inset.

teardrop-like microrobots, a rotating field around the **y** axis is applied, as illustrated in Fig. 5A-I. These microrobots are typical surface walkers, achieving net translation through rolling near the surface [38,39]. The rolling motion is captured in the micrographs of Fig. 5A-I. The microrobot aligns its long axis to the field direction and rotates in the same direction as the field. In contrast, the tadpole-like microrobots are tested in an oscillating magnetic field along the **y** axis within the *XOY* plane, as depicted in Fig. S8. They can swim via the undulation of the tail, exhibiting a maximum velocity of about 110.4 μm/s at 5 Hz. The propulsion of our tadpole-like microrobot during the swimming motion is driven by the deformation of its tail, which is composed of alginate hydrogels cross-linked with calcium ions. These hydrogels exhibit Young's moduli in the range of 100-600 kPa [40], making them suitable for creating deformable microstructures. The tail of the microrobot features a tapered geometry that progressively reduces bending stiffness towards the rear. This design concentrates the deformation at the rear, where the tail is more flexible. Moreover, the tail's high length-to-diameter ratio allows it to bend more easily under the forces generated by the oscillating head. These small deformations contribute to the tadpole-like microrobot's swimming motion.

In comparison to the swimming motion, these microrobots show relatively high locomotion efficiency in the stick-slip motion when in contact with a substrate. Given that most current magnetic microrobots are fabricated using high-density materials, such as high molecular weight polymers, magnetic micro/nanoparticles, and metals, they tend to sink to the substrate bottom. Therefore, interactions with a wall are inevitable for magnetic microrobots during locomotion. Rather than viewing this as a limitation, we leverage these wall interactions to improve our microrobots' locomotion capabilities. Our tadpole-like microrobot exploits these interactions to achieve higher motility in stick-slip motion than its swimming motion. The stick-slip motion is induced under an oscillating field around the **y** at an angle θ of 60° axis within the *YOZ* plane, as clarified in Fig. 5A-II. The magnetic torque lifts the microrobot's head during the first half of the cycle; subsequently, the head descends with the field and strikes the wall boundary in the second half of the cycle. This motion occurs when the contact point between the microrobot and the wall boundary slips, similar to the stick-slip motion observed by Pawashe et al. [41]. The simulated fluid dynamics around the microrobots in rolling and stick-slip motions are depicted in Fig. 5B. During the rolling motion, the flow velocity increases at the front and the rear of the teardrop-like microrobot. Conversely, for the tadpole-like

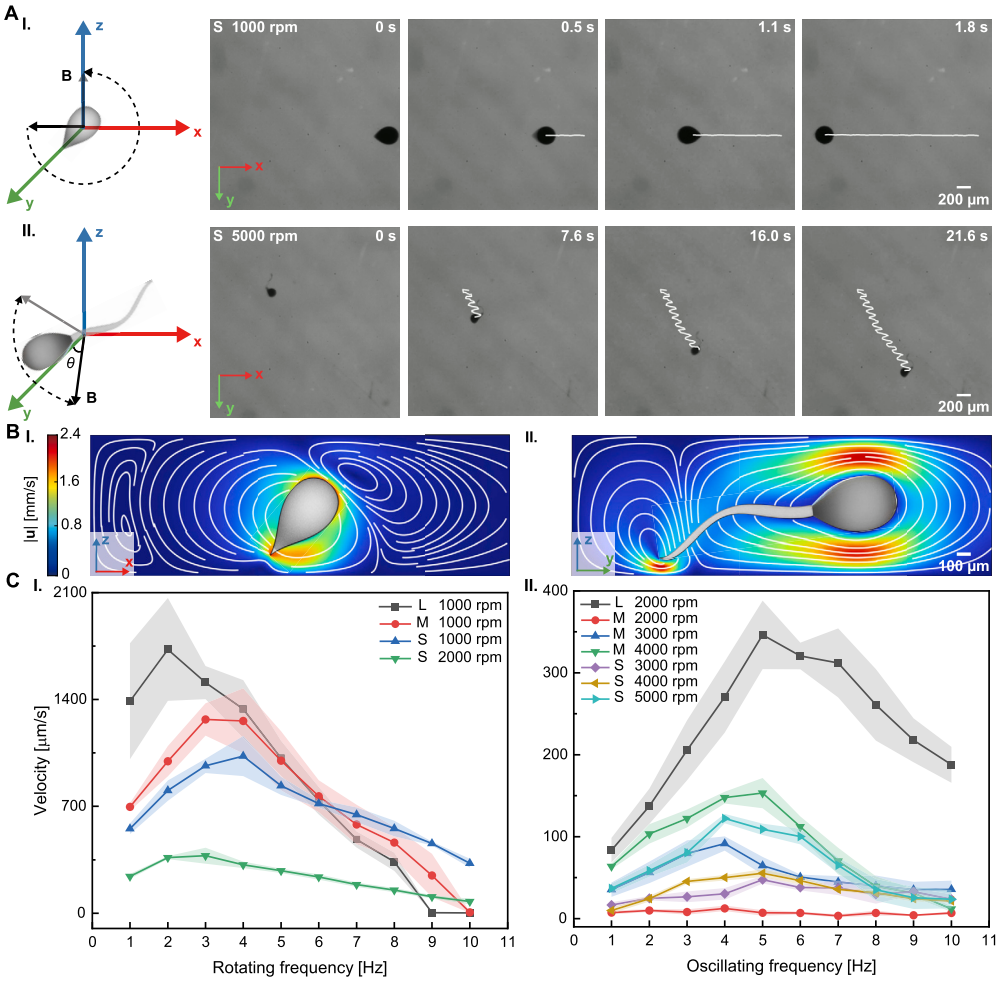

Fig. 5. Locomotion characterization of teardrop-like and tadpole-like microrobots. (A) Time-lapse micrographs of (I) the teardrop-like microrobot's rolling motion under a rotating magnetic field and (II) the tadpole-like microrobot's stick-slip motion under an oscillating magnetic field with an oscillating angle of θ. White curves represent their motion trajectories. (B) Simulated fluid distribution around (I) the teardrop-like microrobot under rolling motion and (II) the tadpole-like microrobot under stick-slip motion (see Materials and Methods). (C) Frequency response curves of (I) teardrop-like microrobots' rolling motion and (II) tadpole-like microrobots' stick-slip motion. The legend describes the corresponding experimental conditions.

microrobot, the maximum flow velocity is observed at its tail end, with considerably lower flow velocity around the head. This suggests that the greater flow velocity at the tail enables the microrobot to move forward during the stick-slip motion.

To clarify the role of the tail in the locomotion, we conduct comparative experiments between the tadpole-like and teardrop-like microrobots during the stick-slip motion. Our findings indicate the velocity along the oscillating axis is negligible for the teardrop-like microrobot, in contrast to the significantly higher velocity observed for the tadpole-like microrobot, as shown in Fig. S9A. Furthermore, we compute the fluid distribution around both microrobots (Fig. S9B). The results demonstrate that the presence of the tail leads to a larger flow velocity at the rear end, underscoring the role of the tail in enhancing locomotion during stick-slip motion. To further investigate the effects of the tail's length, width, and curvature on the rear flow velocity, we conduct simulations to compute the fluid distribution around the microrobots with varying geometric parameters of the tail. Fig. S10A demonstrates that the rear flow velocity increases with the tail length. The higher flow velocity at the tail's rear results in a faster velocity, which corresponds well with our observation that the tadpole-like microrobot exhibits a faster stick-slip motion with a longer tail (Fig. 5C-II). Conversely, variation in the tail width gives rise to negligible changes in the rear flow velocity, as depicted in Fig. S10B. Fig. S10C indicates the effects of the maximum curvature at the rear half of the tail. As the tail's curvature increases, the maximum flow velocity shifts to the tail segment with the maximum curvature, accompanied by a decrease in the rear flow velocity. This reduction might contribute to a decrease in the velocity of the tadpole-like microrobot.

Next, the locomotion ability of each group of magnetic alginate microrobots was quantitatively assessed. During one rotation cycle, the teardrop-like microrobot moves forward at a distance proportional to its perimeter. Therefore, the teardrop-like microrobot's velocity increases with the perimeter size at a constant actuation frequency. This correlation aligns with the experimental results shown in Fig. 5C-I. The teardrop-like microrobots fabricated with the L-sized nozzle show the maximum velocities of 1728 μm/s at 2 Hz. The velocity increases with the frequency and decreases dramatically beyond the step-out frequency [42]. Fig. 5C-I illustrates that teardrop-like microrobots of varying dimensions exhibit distinct step-out frequencies, ranging from 2 to 4 Hz. The tadpole-like microrobots demonstrate considerably lower velocities than the teardrop-like microrobots, yet they exhibit higher step-out frequencies than the latter. Their frequency response curves are displayed in Fig. 5C-II. The tadpole-like microrobots obtained at 2000 rpm using the L-sized nozzle exhibit a maximum velocity of 346 μm/s at 5 Hz. The velocity would increase with the tail length, as demonstrated by the frequency response curves of the tadpole-like microrobots fabricated using the S- and M-sized nozzles. An exception was observed for those produced at 2000 rpm using the M-sized nozzle, which shows nearly zero

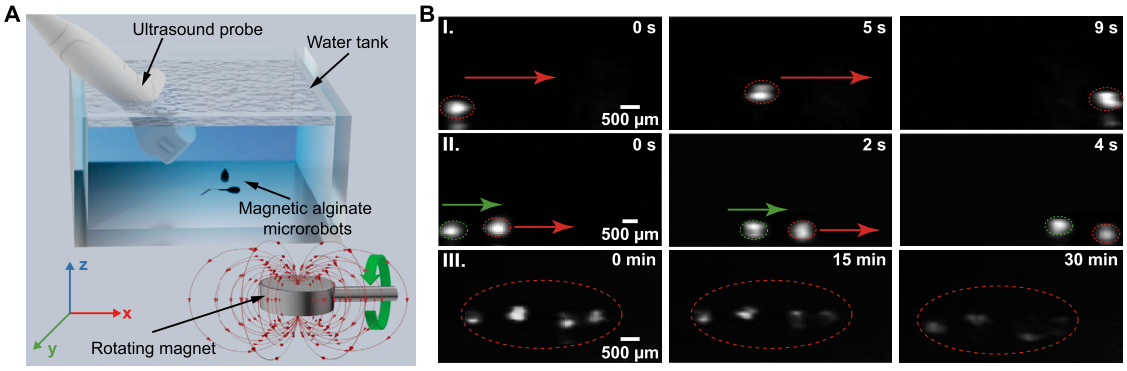

Fig. 6. Ultrasound imaging of magnetic alginate microrobots. (A) Schematic of the experimental setup for magnetic actuation and ultrasound imaging of the microrobots. (B) Time-lapse ultrasound images show (I) the rolling motion of a single microrobot, (II) the rolling motions of two microrobots, and (III) the degradation of multiple microrobots.

velocities. This can be attributed to their respective short tail length (around 85 μm) in contrast to the head size with the average Feret diameter of 280 μm.

A summary of recent magnetic microrobots inspired by sperm, fish, and tadpoles is presented in Table S2 to evaluate the locomotion capabilities of our tadpole-like microrobots. It outlines their fabrication methods, step-out frequencies, maximum velocities, types of motion, and locomotion efficiencies. During the swimming motion, the tadpole-like microrobot achieves a locomotion efficiency of 0.13 body lengths/s through its tail undulation. When it switches to the stick-slip motion, the microrobot can improve the locomotion efficiency to 0.42 body lengths/s. This motion mode employs both the tail undulation and interactions with a wall. The improvement in locomotion efficiency considers practical environments, as most magnetic microrobots are operated close to walls for locomotion and biomedical applications. The locomotion efficiency of our tadpole-like microrobots with the stick-slip motion is comparable to or exceeds that of many existing tadpole-like and sperm-like microrobots. Additionally, our tadpole-like microrobots exhibit a step-out frequency of 5 Hz, which is modest but close to some recent magnetic microrobots inspired by sperm and tadpoles [22,23,43]. For accurate tracking and control, magnetic microrobots are typically actuated below 5 Hz for *in vivo* applications [44–46]. Consequently, our microrobots maintain functional utility in practical biomedical scenarios with a step-out frequency of 5 Hz.

To showcase the capabilities of two distinct motions, we performed obstacle crossing and navigation in constrained spaces on the teardrop-like and tadpole-like microrobots, as illustrated in Fig. S11 and Movie S2. The teardrop-like microrobot utilizes rolling motion to successfully climb over the obstacle, while the tadpole-like microrobot, employing stick-slip motion, is unable to cross (Fig. S11A). Although the teardrop-like microrobots demonstrate obstacle-crossing abilities and higher speeds, they have limitations in environments with vertical constraints due to their rolling motion along their long axis. Each rolling cycle of the teardrop-like microrobots involves a full rotation, which could be restrictive when navigating them in environments with limited vertical space. In contrast, the stick-slip motion of the tadpole-like microrobots does not undergo an entire rotation. This motion pattern and compact design allow them to pass through the vertically constrained channel, as shown in Fig. S11B. Such capability is crucial for potential applications in the cardiovascular system or minimally invasive diagnostics in the gastrointestinal tract, where microrobots must navigate through varied and confined spaces.

3.5. Ultrasound imaging of magnetic alginate microrobots' locomotion and degradation

The locomotion capability of microrobots is a prerequisite for microrobotic systems, tracking microrobots is also important after deployment. The localization of microrobots can be easily achieved through a microscope *in vitro*. However, optical imaging proves ineffective *in vivo* due to its limited ability to penetrate tissue. To overcome this limitation, advanced imaging modalities, such as magnetic resonance imaging (MRI), ultrasound (US) imaging, computed tomography (CT), positron emission tomography (PET), and single-photon emission computed tomography (SPECT) are incorporated into microrobotic systems [47,48]. In this study, a US imaging system was utilized to track the position of the magnetic alginate microrobots, capitalizing on the acoustic impedance mismatch between the microrobot and the surrounding fluid. Magnetic actuation systems, including systems with permanent magnets and systems with electromagnets, are commonly employed to actuate microrobots [49,50]. Considering the specific requirements for a large operational area, permanent magnet systems are favored for *in vivo* applications [51–53]. The experimental setup, which includes a rotating permanent magnet system and a US imaging system, is illustrated and presented in Fig. 6A and Fig. S12.

The locomotion and degradation of the magnetic alginate microrobots were monitored via the US imaging systems (see Materials and Methods, Movies S3, and S4). In the experiment, these microrobots were placed in a water tank, while the US probe was submerged in the water at an angle of 45° [54]. Notably, the teardrop-like microrobots and the tadpole-like microrobots exhibited rolling motion in the presence of the rotating permanent magnet. The US imaging experiments were conducted on the teardrop-like microrobots fabricated at 1000 rpm using the L-sized nozzle, whose average Feret diameter is 649 μm. The US imaging system was operated at its highest frequency of 14 MHz to enable the highest pixel resolution. Time-lapse sequences of the rolling motions of single and two teardrop-like microrobots are presented in Figs. 6B-I and 6B-II. Furthermore, the stability and degradation of the magnetic alginate microrobots were validated in the simulated gastric fluid (pH = 1.2) and the phosphate-buffered saline (PBS) solution (pH = 7.4). Fig. S13 indicates the microrobots can remain intact within the acid fluid for one day and completely degrade in the PBS in one hour. The degradation of the multiple microrobots was captured by the US imaging system, as shown in Fig. 6B-III. The imaging signal intensity of the microrobots weakens over time, implying their degradation. After 20 min, the weak imaging signal can still be observed. This is because the clusters of magnetic nanoparticles remain adhered to the substrate after the degradation of the alginate hydrogel. The degradation can be attributed to the swelling of the alginate particles in the PBS solution [55], offering the potential to achieve drug release using these alginate microrobots. Moreover, the stability in acidic fluids can ensure the microrobots' integrity when passing through the stomach, making them suitable for use in orally administered pharmaceutical pills [56].

4. Conclusion

In summary, we present a simple and high-throughput fabrication method for constructing magnetic alginate microrobots, including teardrop-like and tadpole-like microrobots, using a centrifugally driven flow. The dimensions of the teardrop-like microrobots can be adjusted by tuning the nozzle diameters, while the tail lengths of the tadpole-like microrobots vary with the revolution speeds. Our simulation results reveal that the extruded flow velocity varies with the nozzle diameters and revolution speeds, enabling customization of the microrobots' shapes and dimensions. A quantitative analysis of the microrobots' dimensions is thoroughly performed and validated against experimental measurements. Moreover, the teardrop-like and tadpole-like microrobots can exhibit rolling and stick-slip motion by programming the external fields to capitalize on their different morphologies. The dual-motion patterns of our microrobots enable them to perform different tasks, including obstacle crossing and navigation in vertically constrained spaces. Moreover, the tadpole-like microrobots achieve locomotion performance comparable to or better than some of the more complex and costly bioinspired magnetic microrobots. Last, the locomotion and degradation of these microrobots are successfully detected with a clinical US imaging system. The biodegradability of our microrobots opens up possibilities for cargo/drug delivery, as cargo or drugs can be encapsulated within the microrobots during fabrication and released after complete degradation. This feature, combined with their dual-motion patterns and efficient locomotion, positions our microrobots as versatile tools for various biomedical applications.

In addition to alginate sodium, the proposed fabrication method is versatile in material selection. It can employ any monomer that undergoes a sol-gel transition when exposed to liquid crosslinkers. This adaptability enables the incorporation of specialized functional materials, designed to fulfill the specific functionalities of microrobots. Nevertheless, our current work needs further exploration. While the comparable locomotion efficiency of our microrobots to existing sperm-like and tadpole-like microrobots, our results indicate a step-out frequency of 5 Hz. Given that most previous studies on the wireless actuation of microrobots have been conducted below their step-out frequencies, increasing the step-out frequency of our microrobots is crucial. Strategies to achieve this include increasing the strength of the applied magnetic field, using high-magnetization materials, and modifying the surface wettability of the microrobots. Furthermore, the teardrop and tadpole contours have been known to reduce fluidic drag during translating motion. The motion modes presented in our study do not fully capitalize on this streamlined contour of the microrobots, as the fluid flow does not consistently move smoothly around the streamlined contour during locomotion. This indicates the necessity for additional research to investigate how these streamlined contours can be better utilized to enhance locomotion efficiency or upstream motility. In future research, we can explore these effects by employing the actuation of magnetic force or catalytic reaction to achieve translating motion.

CRediT authorship contribution statement

Zihan Wang: Writing – original draft, Validation, Methodology, Investigation, Formal analysis, Conceptualization. **Wenjian Li:** Writing – review & editing, Investigation. **Chuang Li:** Writing – review & editing, Investigation. **Anke Klingner:** Writing – review & editing, Software. **Yutao Pei:** Writing – review & editing. **Sarthak Misra:** Writing – review & editing, Funding acquisition. **Islam S.M. Khalil:** Writing – review & editing, Supervision, Project administration.

Declaration of competing interest

The authors declare that they have no known competing financial interests or personal relationships that could have appeared to influence the work reported in this paper.

Data availability

Data will be made available on request.

Acknowledgements

This work is supported by the European Research Council (ERC) under the European Union's Horizon 2020 Research and Innovation programme under Grant 866494 project-MAESTRO and the China Scholarship Council under Grant No. 202006120058.

Appendix A. Supplementary material

Supplementary material related to this article can be found online at https://doi.org/10.1016/j.matdes.2024.113337.

References

[1] B.J. Nelson, S. Pané, Delivering drugs with microrobots, Science 382 (2023) 1120–1122, https://doi.org/10.1126/science.adh3073.
[2] B.J. Nelson, I.K. Kaliakatsos, J.J. Abbott, Microrobots for minimally invasive medicine, Annu. Rev. Biomed. Eng. 12 (2010) 55–85, https://doi.org/10.1146/annurev-bioeng-010510-103409.
[3] X. Peng, M. Urso, M. Kolackova, D. Huska, M. Pumera, Biohybrid magnetically driven microrobots for sustainable removal of micro/nanoplastics from the aquatic environment, Adv. Funct. Mater. 34 (2024) 2307477, https://doi.org/10.1002/adfm.202307477.
[4] C.C. Mayorga-Martinez, M. Fojtů, J. Vyskočil, N.-J. Cho, M. Pumera, Pollen-based magnetic microrobots are mediated by electrostatic forces to attract, manipulate, and kill cancer cells, Adv. Funct. Mater. 32 (2022) 2207272, https://doi.org/10.1002/adfm.202207272.
[5] S. Xu, J. Liu, C. Yang, X. Wu, T. Xu, A learning-based stable servo control strategy using broad learning system applied for microrobotic control, IEEE Trans. Cybern. 52 (2022) 13727–13737, https://doi.org/10.1109/TCYB.2021.3121080.
[6] S. Zhong, Y. Hou, Q. Shi, Y. Li, H.-W. Huang, Q. Huang, T. Fukuda, H. Wang, Spatial constraint-based navigation and emergency replanning adaptive control for magnetic helical microrobots in dynamic environments, IEEE Trans. Autom. Sci. Eng. (2023) 1–10, https://doi.org/10.1109/TASE.2023.3339637.
[7] H. Wang, S. Zhong, Z. Zheng, Q. Shi, T. Sun, Q. Huang, T. Fukuda, Data-driven parallel adaptive control for magnetic helical microrobots with derivative structure in uncertain environments, IEEE Trans. Syst. Man Cybern. Syst. 54 (2024) 4139–4150, https://doi.org/10.1109/TSMC.2024.3374071.
[8] Y. Liu, H. Chen, Q. Zou, X. Du, Y. Wang, J. Yu, Automatic navigation of microswarms for dynamic obstacle avoidance, IEEE Trans. Robot. 39 (2023) 2770–2785, https://doi.org/10.1109/TRO.2023.3263773.
[9] R.K. Harrison, Phase ii and phase iii failures: 2013–2015, Nat. Rev. Drug Discov. 15 (2016) 817–818, https://doi.org/10.1038/nrd.2016.184.
[10] J. Aparicio-Blanco, N. Vishwakarma, C.-M. Lehr, C.A. Prestidge, N. Thomas, R.J. Roberts, C.R. Thorn, A. Melero, Antibiotic resistance and tolerance: what can drug delivery do against this global threat?, Drug Deliv. Transl. Res. (2024), https://doi.org/10.1007/s13346-023-01513-6.
[11] S. Senapati, A.K. Mahanta, S. Kumar, P. Maiti, Controlled drug delivery vehicles for cancer treatment and their performance, Signal Transduct. Targeted Ther. 3 (2018) 7, https://doi.org/10.1038/s41392-017-0004-3.
[12] U. Bozuyuk, P. Wrede, E. Yildiz, M. Sitti, Roadmap for clinical translation of mobile microrobotics, Adv. Mater. (2024) 2311462, https://doi.org/10.1002/adma.202311462.
[13] H. Wang, M. Pumera, Fabrication of micro/nanoscale motors, Chem. Rev. 115 (2015) 8704–8735, https://doi.org/10.1021/acs.chemrev.5b00047.
[14] S. Palagi, P. Fischer, Bioinspired microrobots, Nat. Rev. Mater. 3 (2018) 113–124, https://doi.org/10.1038/s41578-018-0016-9.
[15] Z. Wang, A. Klingner, V. Magdanz, S. Misra, I.S.M. Khalil, Soft bio-microrobots: toward biomedical applications, Adv. Intell. Syst. 6 (2024) 2300093, https://doi.org/10.1002/aisy.202300093.
[16] C. Huang, Z. Lai, L. Zhang, X. Wu, T. Xu, A magnetically controlled soft miniature robotic fish with a flexible skeleton inspired by zebrafish, Bioinspir. Biomim. 16 (2021) 065004, https://doi.org/10.1088/1748-3190/ac23a9.
[17] J. Leclerc, H. Zhao, D. Bao, A.T. Becker, In vitro design investigation of a rotating helical magnetic swimmer for combined 3-d navigation and blood clot removal, IEEE Trans. Robot. 36 (2020) 975–982, https://doi.org/10.1109/TRO.2020.2988636.
[18] H.-W. Huang, M.S. Sakar, A.J. Petruska, S. Pané, B.J. Nelson, Soft micromachines with programmable motility and morphology, Nat. Commun. 7 (2016) 12263, https://doi.org/10.1038/ncomms12263.
[19] B.J. Williams, S.V. Anand, J. Rajagopalan, M.T.A. Saif, A self-propelled biohybrid swimmer at low Reynolds number, Nat. Commun. 5 (2014) 3081, https://doi.org/10.1038/ncomms4081.

[20] T. Li, J. Li, H. Zhang, X. Chang, W. Song, Y. Hu, G. Shao, E. Sandraz, G. Zhang, L. Li, J. Wang, Magnetically propelled fish-like nanoswimmers, Small 12 (2016) 6098–6105, https://doi.org/10.1002/smll.201601846.
[21] C. Xin, D. Jin, Y. Hu, L. Yang, R. Li, L. Wang, Z. Ren, D. Wang, S. Ji, K. Hu, D. Pan, H. Wu, W. Zhu, Z. Shen, Y. Wang, J. Li, L. Zhang, D. Wu, J. Chu, Environmentally adaptive shape-morphing microrobots for localized cancer cell treatment, ACS Nano 15 (2021) 18048–18059, https://doi.org/10.1021/acsnano.1c06651.
[22] M. You, F. Mou, K. Wang, J. Guan, Tadpole-like flexible microswimmers with the head and tail both magnetic, ACS Appl. Mater. Interfaces 15 (2023) 40855–40863, https://doi.org/10.1021/acsami.3c09701.
[23] R. Tan, X. Yang, H. Lu, Y. Shen, One-step formation of polymorphous sperm-like microswimmers by vortex turbulence-assisted microfluidics, Nat. Commun. 15 (2024) 4761, https://doi.org/10.1038/s41467-024-49043-0.
[24] I.S.M. Khalil, A. Fatih Tabak, A. Klingner, M. Sitti, Magnetic propulsion of robotic sperms at low-Reynolds number, Appl. Phys. Lett. 109 (2016) 033701, https://doi.org/10.1063/1.4958737.
[25] G. Velve-Casquillas, M. Le Berre, M. Piel, P.T. Tran, Microfluidic tools for cell biological research, Nano Today 5 (2010) 28–47, https://doi.org/10.1016/j.nantod.2009.12.001.
[26] E. Livak-Dahl, I. Sinn, M. Burns, Microfluidic chemical analysis systems, Annu. Rev. Chem. Biomol. Eng. 2 (2011) 325–353, https://doi.org/10.1146/annurev-chembioeng-061010-114215.
[27] P. Yager, T. Edwards, E. Fu, K. Helton, K. Nelson, M.R. Tam, B.H. Weigl, Microfluidic diagnostic technologies for global public health, Nature 442 (2006) 412–418, https://doi.org/10.1038/nature05064.
[28] S. Bahrami, N. Baheiraei, M. Najafi-Ashtiani, S. Nour, M. Razavi, Chapter 9 - microfluidic devices in tissue engineering, in: M.R. Hamblin, M. Karimi (Eds.), Biomedical Applications of Microfluidic Devices, Academic Press, 2021, pp. 209–233.
[29] A.W. Adamson, A.P. Gast, Physical Chemistry of Surfaces, 6th ed., John Wiley and Sons, New York, NY, 1997.
[30] K.Y. Lee, D.J. Mooney, Alginate: properties and biomedical applications, Prog. Polym. Sci. 37 (2012) 106–126, https://doi.org/10.1016/j.progpolymsci.2011.06.003.
[31] S. Groß, V. Reichelt, A. Reusken, A finite element based level set method for two-phase incompressible flows, Comput. Vis. Sci. 9 (2006) 239–257, https://doi.org/10.1007/s00791-006-0024-y.
[32] W. Doherty, T.N. Phillips, Z. Xie, A stabilised finite element framework for viscoelastic multiphase flows using a conservative level-set method, J. Comput. Phys. 477 (2023) 111936, https://doi.org/10.1016/j.jcp.2023.111936.
[33] G.-H. Cottet, E. Maitre, T. Milcent, Level Set Methods for Fluid-Structure Interaction, Springer Nature, 2022.
[34] J.A. Sethian, P. Smereka, Level set methods for fluid interfaces, Annu. Rev. Fluid Mech. 35 (2003) 341–372, https://doi.org/10.1146/annurev.fluid.35.101101.161105.
[35] E. Olsson, G. Kreiss, A conservative level set method for two phase flow, J. Comput. Phys. 210 (2005) 225–246, https://doi.org/10.1016/j.jcp.2005.04.007.
[36] A.S. Utada, E. Lorenceau, D.R. Link, P.D. Kaplan, H.A. Stone, D.A. Weitz, Monodisperse double emulsions generated from a microcapillary device, Science 308 (2005) 537–541, https://doi.org/10.1126/science.1109164.
[37] S. Haeberle, L. Naegele, R. Burger, F. v. Stetten, R. Zengerle, J. Ducree, Alginate bead fabrication and encapsulation of living cells under centrifugally induced artificial gravity conditions, J. Microencapsul. 25 (2008) 267–274, https://doi.org/10.1080/02652040801954333.
[38] W.-Z. Fang, S. Ham, R. Qiao, W.-Q. Tao, Magnetic actuation of surface walkers: the effects of confinement and inertia, Langmuir 36 (2020) 7046–7055, https://doi.org/10.1021/acs.langmuir.9b03487.
[39] P. Tierno, R. Golestanian, I. Pagonabarraga, F. Sagués, Controlled swimming in confined fluids of magnetically actuated colloidal rotors, Phys. Rev. Lett. 101 (2008) 218304, https://doi.org/10.1103/PhysRevLett.101.218304.
[40] G. Kaklamani, D. Cheneler, L.M. Grover, M.J. Adams, J. Bowen, Mechanical properties of alginate hydrogels manufactured using external gelation, J. Mech. Behav. Biomed. Mater. 36 (2014) 135–142, https://doi.org/10.1016/j.jmbbm.2014.04.013.
[41] C. Pawashe, S. Floyd, M. Sitti, Dynamic modeling of stick slip motion in an untethered magnetic micro-robot, in: Robotics: Science and Systems IV, MIT Press, Cambridge, MA, 2009.
[42] A.W. Mahoney, N.D. Nelson, K.E. Peyer, B.J. Nelson, J.J. Abbott, Behavior of rotating magnetic microrobots above the step-out frequency with application to control of multi-microrobot systems, Appl. Phys. Lett. 104 (2014) 144101, https://doi.org/10.1063/1.4870768.
[43] V. Magdanz, I.S.M. Khalil, J. Simmchen, G.P. Furtado, S. Mohanty, J. Gebauer, H. Xu, A. Klingner, A. Aziz, M. Medina-Sánchez, O.G. Schmidt, S. Misra, Ironsperm: sperm-templated soft magnetic microrobots, Sci. Adv. 6 (2020) eaba5855, https://doi.org/10.1126/sciadv.aba5855.
[44] B. Wang, Q. Wang, K.F. Chan, Z. Ning, Q. Wang, F. Ji, H. Yang, S. Jiang, Z. Zhang, B.Y.M. Ip, H. Ko, J.P.W. Chung, M. Qiu, J. Han, P.W.Y. Chiu, J.J.Y. Sung, S. Du, T.W.H. Leung, S.C.H. Yu, L. Zhang, tPA-anchored nanorobots for in vivo arterial recanalization at submillimeter-scale segments, Sci. Adv. 10 (2024) eadk8970, https://doi.org/10.1126/sciadv.adk8970.
[45] H. Zhang, Z. Li, C. Gao, X. Fan, Y. Pang, T. Li, Z. Wu, H. Xie, Q. He, Dual-responsive biohybrid neutrobots for active target delivery, Sci. Robot. 6 (2021) eaaz9519, https://doi.org/10.1126/scirobotics.aaz9519.
[46] B. Wang, K.F. Chan, K. Yuan, Q. Wang, X. Xia, L. Yang, H. Ko, Y.-X.J. Wang, J.J.Y. Sung, P.W.Y. Chiu, L. Zhang, Endoscopy-assisted magnetic navigation of biohybrid soft microrobots with rapid endoluminal delivery and imaging, Sci. Robot. 6 (2021) eabd2813, https://doi.org/10.1126/scirobotics.abd2813.
[47] B. Wang, Y. Zhang, L. Zhang, Recent progress on micro- and nano-robots: towards in vivo tracking and localization, Quant. Imaging Med. Surg. 8 (2018) 461–479, https://doi.org/10.21037/qims.2018.06.07.
[48] A. Aziz, S. Pane, V. Iacovacci, N. Koukourakis, J. Czarske, A. Menciassi, M. Medina-Sánchez, O.G. Schmidt, Medical imaging of microrobots: toward in vivo applications, ACS Nano 14 (2020) 10865–10893, https://doi.org/10.1021/acsnano.0c05530.
[49] Z. Yang, L. Zhang, Magnetic actuation systems for miniature robots: a review, Adv. Intell. Syst. 2 (2020) 2000082, https://doi.org/10.1002/aisy.202000082.
[50] H. Zhou, C.C. Mayorga-Martinez, S. Pané, L. Zhang, M. Pumera, Magnetically driven micro and nanorobots, Chem. Rev. 121 (2021) 4999–5041, https://doi.org/10.1021/acs.chemrev.0c01234.
[51] Y. Kim, E. Genevriere, P. Harker, J. Choe, M. Balicki, R.W. Regenhardt, J.E. Vranic, A.A. Dmytriw, A.B. Patel, X. Zhao, Telerobotic neurovascular interventions with magnetic manipulation, Sci. Robot. 7 (2022) eabg9907, https://doi.org/10.1126/scirobotics.abg9907.
[52] L. Su, D. Jin, Y. Wang, Q. Wang, C. Pan, S. Jiang, H. Yang, Z. Yang, X. Wang, N. Xia, K.F. Chan, P.W.Y. Chiu, J.J.-Y. Sung, L. Zhang, Modularized microrobot with lock-and-detachable modules for targeted cell delivery in bile duct, Sci. Adv. 9 (2023) eadj0883, https://doi.org/10.1126/sciadv.adj0883.
[53] D. Jin, Q. Wang, K.F. Chan, N. Xia, H. Yang, Q. Wang, S.C.H. Yu, L. Zhang, Swarming self-adhesive microgels enabled aneurysm on-demand embolization in physiological blood flow, Sci. Adv. 9 (2023) eadf9278, https://doi.org/10.1126/sciadv.adf9278.
[54] C. Li, S. Misra, I.S.M. Khalil, Closed-loop control characterization of untethered small-scale helical device in physiological fluid with dynamic flow rates, Adv. Intell. Syst. 5 (2023) 2200322, https://doi.org/10.1002/aisy.202200322.
[55] S. Bajpai, S. Sharma, Investigation of swelling/degradation behavior of alginate beads crosslinked with Ca^{2+} and Ba^{2+} ions, React. Funct. Polym. 59 (2004) 129–140, https://doi.org/10.1016/j.reactfunctpolym.2004.01.002.
[56] R. Mundaca-Uribe, N. Askarinam, R.H. Fang, L. Zhang, J. Wang, Towards multifunctional robotic pills, Nat. Biomed. Eng. (2023), https://doi.org/10.1038/s41551-023-01090-6.